

**First results from a search for axionlike dark matter using
octupole-deformed nuclei in a crystal**

Mingyu Fan, Bassam Nima, Aleksandar Radak,
Gonzalo Alonso-Álvarez, and Amar Vutha

University of Toronto, 60 St. George Street, Toronto ON M5S 1A7, Canada

arXiv:2410.02218v1 [physics.atom-ph] 3 Oct 2024

Abstract

Most of the matter in the universe is in the form of dark matter. However, dark matter has never been observed to interact with normal matter in laboratory experiments. ALPs – ultralight axionlike particles – are a class of dark matter models that are consistent with astrophysical constraints, and produce measurable signatures in the form of oscillating violations of discrete symmetries in nuclei. We report the first results from a search for oscillating parity-odd time-reversal-odd nuclear moments of ^{153}Eu ions in a crystal, which leads to an experimental constraint on the ALP-gluon coupling strength across a wide band of ALP masses.

Astrophysical observations indicate that the majority of matter in the universe is dark matter [1]. However, dark matter has only been observed to interact gravitationally with ordinary matter, and no other interactions with Standard Model particles have been measured [2].

Out of the many models for the cold dark matter within galaxies, ultralight axionlike particles (ALPs) are a well-motivated and viable subset [3–5]. When ALPs interact with gluons within atomic nuclei, they induce nuclear moments that are odd under parity (P) and time-reversal (T) symmetries, and that oscillate in time [6]. Experiments sensitive to P-odd T-odd nuclear moments – such as searches for permanent electric dipole moments (EDMs) of particles – can detect these oscillations. For example, broadband laboratory bounds on the ALP-gluon coupling strength in the mass range below 3×10^{-12} eV have been obtained from neutron EDM experiments [7, 8]. The HfF^+ electron EDM experiment [9] and a series of frequency comparison experiments [10–16] also provide bounds, which, although less stringent than the bounds from neutron EDM experiments, nevertheless offer useful cross-checks using different physical systems.

In this work, we probe oscillatory P-odd T-odd nuclear moments using precision spectroscopy of octupole-deformed nuclei in a crystal (ONIX). Our measurement method builds upon the search for static nuclear T-violation proposed in Ref. [17]. We use europium-153 (nuclear spin $I = 5/2$), a stable isotope with an octupole-deformed nucleus that has a large, collectively enhanced, P-odd T-odd nuclear Schiff moment induced by ALPs [18, 19].

Triply-charged europium ions doped into a yttrium orthosilicate crystal (Eu:YSO)

are located at non-centrosymmetric crystal sites, where their charge distribution is strongly electrically polarized by the neighboring ions in the crystal. In these trapped, polarized europium ions, the Schiff moment interacts with the electron density gradient near the nucleus, causing nuclear spin states to shift in energy. These characteristic energy shifts depend on the relative orientation of the nuclear spin vector, \vec{I} , and the electric dipole moment of the polarized atom, \vec{D} . Observation of an *oscillating* energy shift proportional to $\vec{I} \cdot \hat{D}$ is the signature of an oscillatory P-odd T-odd nuclear moment, such as would be produced by ALPs.

Crucially, Eu:YSO contains an equal number of Eu^{3+} sites with oppositely-directed \vec{D} vectors, distributed throughout the crystal. These sets of oppositely-polarized ions form two ensembles whose ALP-induced energy shifts oscillate precisely out of phase. Meanwhile, the shifts of these two ensembles due to magnetic fields (including stray fields and spurious backgrounds) are identical and in phase. Therefore comparing measurements between the oppositely-polarized ions provides an accurate means to separate ALP signals from magnetic-field-induced systematic errors [20].

Furthermore, the narrow ${}^7F_0 \rightarrow {}^5D_0$ transition of Eu^{3+} enables optical state control of the europium ions, which leads to fast state preparation, low-noise readout of the nuclear spin states, and simultaneous interrogation of the oppositely-polarized ensembles. Finally, the large number of Eu^{3+} ions in available in the crystal results in high sensitivity to ALP signals.

To quantify the above discussion, we note that ALPs result in a time-varying value of the dimensionless $\bar{\theta}$ parameter of quantum chromodynamics (QCD) [6].

$$\bar{\theta}(t) = \frac{C_G a_0}{f_a} \sin\left(\frac{m_a c^2}{\hbar} t\right). \quad (1)$$

Here C_G is the gluon coupling constant ($C_G = 1$ for the QCD axion) [9], a_0 is the ALP field amplitude, f_a is the ultra-high energy scale associated with ALP formation, and m_a is the ALP mass [6]. The $\bar{\theta}$ parameter in turn creates a nuclear Schiff moment in ${}^{153}\text{Eu}$ given by

$$\vec{\mathcal{S}}(t) = \mathcal{S}_{\bar{\theta}} \frac{\vec{I}}{|I|} \bar{\theta}(t), \quad (2)$$

where $\mathcal{S}_{\bar{\theta}}$ is the ${}^{153}\text{Eu}$ Schiff moment per unit $\bar{\theta}$ [18, 19].

In an electrically polarized Eu^{3+} ion with dipole moment \vec{D} , the effective Hamiltonian describing the T-odd energy shifts of the nuclear spin states is $\mathcal{H}_{\text{ALP}} = -d_{\mathcal{J}} \vec{\mathcal{J}} \cdot \vec{\mathcal{E}}_{\text{eq}}$, where $d_{\mathcal{J}} = 0.33 \times 10^{-17} \text{ e cm}/e \text{ fm}^3$ is the ratio of the permanent atomic EDM to the nuclear Schiff moment for Eu^{3+} [4], and $\vec{\mathcal{E}}_{\text{eq}}$ is the *equivalent electric field* that would have to be applied to the ion to induce in it a dipole moment \vec{D} . The magnitude of the equivalent electric field for the polarized Eu^{3+} ions in Eu:YSO crystal is estimated to be $\mathcal{E}_{\text{eq}} = 1.5 \text{ GV/cm}$ (see Supplemental Material Section I), aligned along the $D1$ axis of the YSO crystal (denoted as \hat{x} in the following).

Combining the equations above, the effective Hamiltonian for the nuclear spin states is

$$\begin{aligned} \mathcal{H}_{\text{ALP}}(t) &= (h \times 400 \text{ kHz}) \left(\frac{\mathcal{I}_{\bar{\theta}}}{1 \text{ e fm}^3} \right) \left(\frac{\mathcal{E}_{\text{eq}}}{1.5 \text{ GV/cm}} \right) \frac{(\vec{I} \cdot \hat{x})(\vec{D} \cdot \hat{x})}{|I|} \bar{\theta}(t), \\ &= h W_T (\vec{I} \cdot \hat{x})(\vec{D} \cdot \hat{x}). \end{aligned} \quad (3)$$

In our experiment, the P-odd T-odd frequency shift due to $\mathcal{H}_{\text{ALP}}(t)$ is measured. The oscillating part of this frequency shift yields the ALP-gluon coupling strength C_G/f_a .

A schematic diagram of the experiment is shown in Fig. 1, and Fig. 2 shows the relevant energy levels and their labels. Measurements were made on a YSO crystal doped with $^{153}\text{Eu}^{3+}$ at 0.01% concentration. The crystal, $3.5 \text{ mm} \times 4.0 \text{ mm} \times 5.0 \text{ mm}$, was attached to a cold plate and maintained at 5 K. A pair of copper plates adjacent to the crystal were used to apply an electric field, \mathcal{E}_{dc} , along the \hat{x} axis. A coil was used to generate radio-frequency (rf) magnetic fields along the \hat{z} axis (parallel to the b axis of the crystal). This doubly-resonant coil was used to apply rf fields in a band around 119.2 MHz to drive the $(a, \bar{a}) \leftrightarrow (b, \bar{b})$ nuclear spin transition in the 7F_0 electronic ground state for state preparation, and to apply fields in a band around 141 kHz to drive the $b \leftrightarrow \bar{b}$ transition for precision spectroscopy. SmCo permanent magnets were used to apply a static magnetic field $\mathcal{B}_{\text{dc}} \approx 225 \text{ G}$ across the Eu:YSO crystal; we chose this value of \mathcal{B}_{dc} in order to adequately separate the $a - b$ and $\bar{a} - \bar{b}$ resonances around 119.2 MHz.

We probed ions at “site 1” in Eu:YSO, where the ${}^7F_0 \rightarrow {}^5D_0$ optical transition is at 580.04 nm [22]. The inhomogeneously-broadened linewidth of the optical transition in our sample was 700 MHz, and the linewidth of the spectral anti-holes used for our

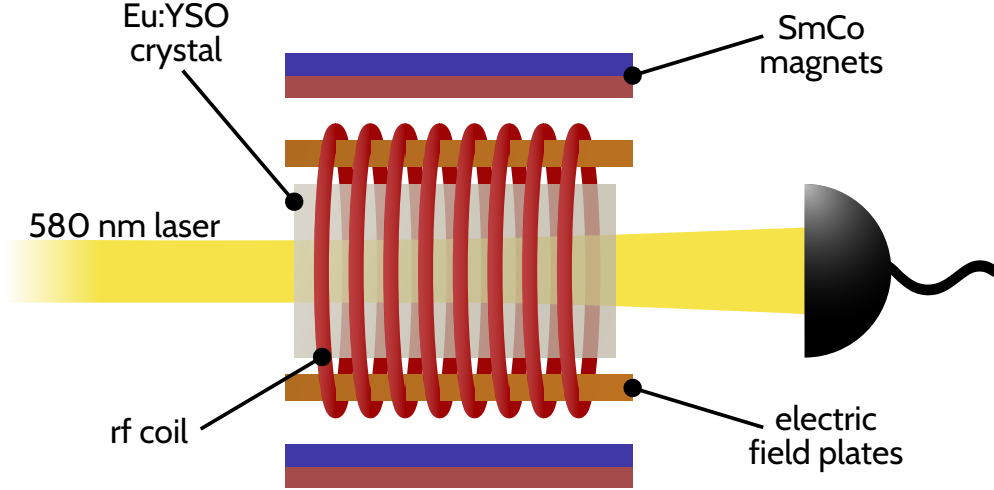


FIG. 1. Apparatus schematic. Data was taken using laser absorption spectroscopy of the ${}^7F_0 \rightarrow {}^5D_0$ transition in a Eu:YSO crystal, held at 5 K. The crystal was placed between a pair of electric field plates, contained within an rf magnetic field coil. A static magnetic field parallel to the electric field was applied using SmCo permanent magnets. The electric field and magnetic field direction is along the crystal D1 axis. The laser propagates through the crystal b axis and is polarized along the D1 axis.

measurements were typically 1 MHz. When an electric field is applied to the crystal, the spectral anti-holes for the oppositely-polarized ion ensembles shift in opposite directions, by an amount proportional to their respective orientations relative to the crystal axis, $\mathcal{D} = \hat{D} \cdot \hat{x} = \pm 1$. We used an electric field $\mathcal{E}_{\text{dc}} = 125 \text{ V cm}^{-1}$, which produces a spectral shift $\Delta\nu = \mp 3.3 \text{ MHz}$ [3] for the $\mathcal{D} = \pm 1$ ensembles, to distinguish the optical absorption features from oppositely-polarized ions and extract W_T .

The experiment sequence begins with an optical pumping pulse that sweeps through the ${}^7F_0 a, \bar{a} \rightarrow {}^5D_0 c', \bar{c}'$ resonance [9]. This pulse clears out the population of spectroscopic classes that are unused in the experiment, and creates a flat background for absorption measurements. Next, \mathcal{E}_{dc} is turned on, and optical pulses tuned to the ${}^7F_0 a, \bar{a} \rightarrow {}^5D_0 c', \bar{c}'$ and ${}^7F_0 c, \bar{c} \rightarrow {}^5D_0 b', \bar{b}'$ resonances pump ions into the ${}^7F_0 b, \bar{b}$ states using the spectral hole burning methods described in Refs. [9, 25]. The electric field is turned off for the subsequent steps, so that the optical absorption features from the $\mathcal{D} = \pm 1$ ions become separated by 6.6 MHz and can be separately measured. Optical probe pulses tuned to the ${}^7F_0 a, \bar{a} \rightarrow {}^5D_0 c', \bar{c}'$, $\mathcal{D} = \pm 1$ resonances determine the background absorption level through the crystal for normalization. An adiabatic rf sweep across the $b \leftrightarrow a$ transition moves ions out of the b state, leaving ions initialized in the

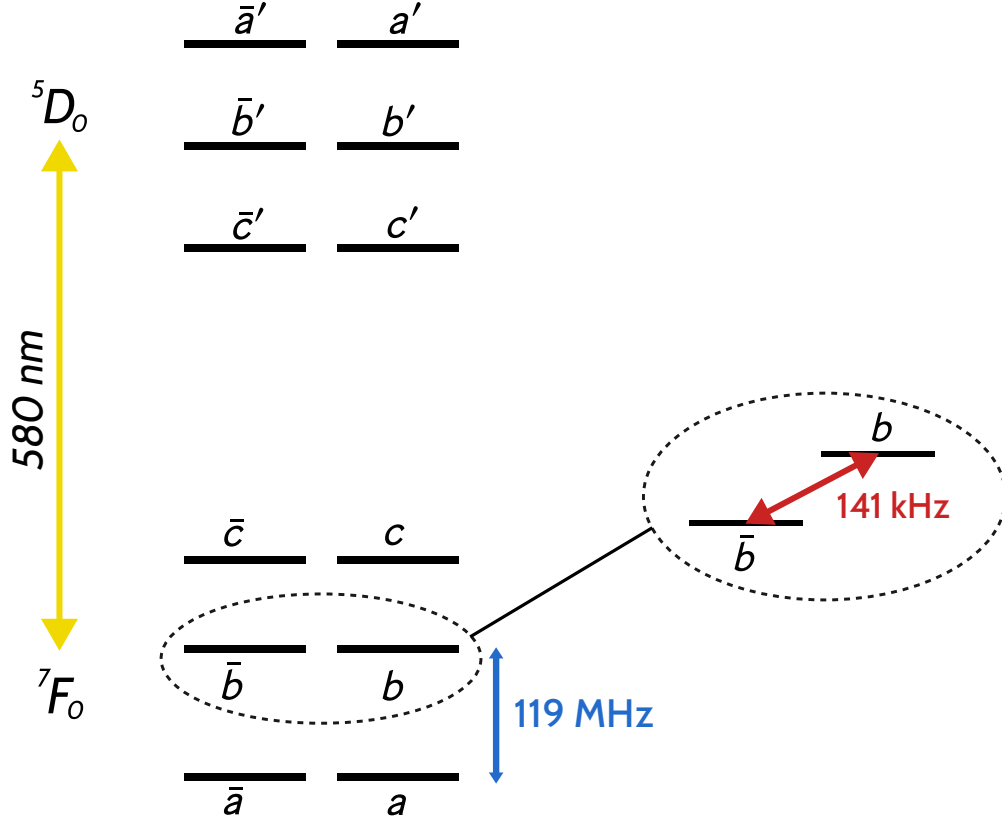


FIG. 2. Energy levels of $^{153}\text{Eu}^{3+}:\text{YSO}$. The ground 7F_0 and excited 5D_0 electronic states are connected by a 580 nm optical transition. Within each electronic state, the 6 nuclear spin sublevels are split into Kramers doublets, with opposite nuclear spin orientations for the two states in each doublet. In the static magnetic field used in this work, the $b \leftrightarrow \bar{b}$ nuclear spin transition at 141 kHz was probed using precision rf spectroscopy.

\bar{b} state.

Two rf $\pi/2$ spectroscopy pulses at a carrier frequency f , separated by $T = 400 \mu\text{s}$ and with a relative phase ϕ_{rf} , are applied to drive the $b \leftrightarrow \bar{b}$ transition. We then apply a second adiabatic sweep over the $b \leftrightarrow a$ transition, which transfers the ions in b to a . Finally, optical probe pulses tuned to 7F_0 $a, \bar{a} \rightarrow {}^5D_0$ c', \bar{c}' , $\mathcal{D} = \pm 1$ are used to measure absorption lines as before, yielding a signal $A(f, \phi_{\text{rf}})$ proportional to the population transferred to the b state by the spectroscopy pulses. A timing diagram of the measurement sequence is shown in Fig. 3.

To precisely measure the $b - \bar{b}$ resonance frequency, $f_0(b\bar{b})$, we use a modified Ramsey method that yields improved control over systematic errors [26–28]. In each cycle, we perform measurements for 8 different values of ϕ_{rf} between 0 and 2π . The corresponding absorption signal, $A(f, \phi_{\text{rf}}) \propto \cos \{ \phi_{\text{rf}} + 2\pi [f - f_0(b\bar{b})] T \}$ versus ϕ_{rf} , is fit to

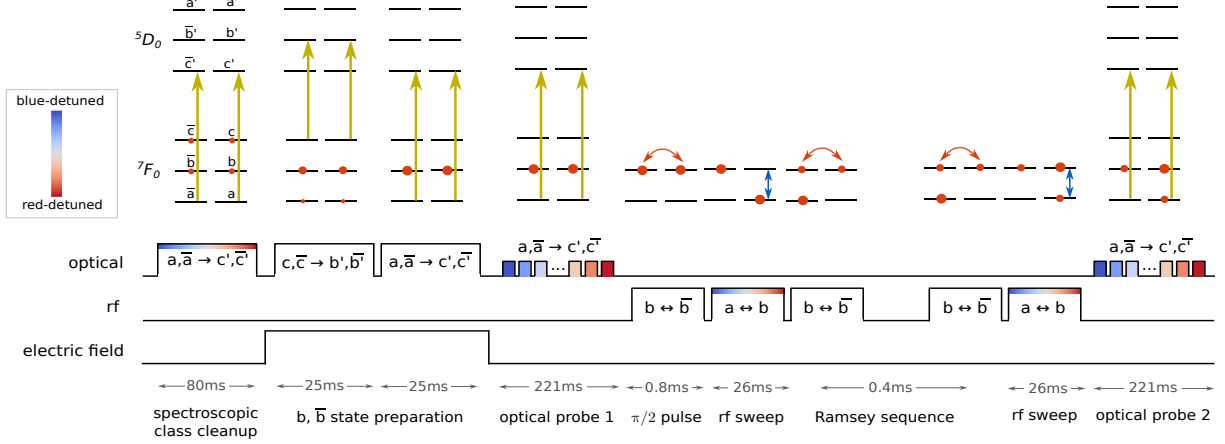


FIG. 3. Pulse sequence for the measurements. The top panel shows the hyperfine levels of the 7F_0 and 5D_0 states and the transitions driven in each step. Yellow arrows drive optical pumping and absorption probe transitions, blue arrows drive rf transitions between hyperfine states ($a \leftrightarrow b$), and orange arrows drive the $b \leftrightarrow \bar{b}$ transition. The bottom panel shows the optical, rf, and electric field pulses corresponding to the top panel. Colors depicts the frequency detunings from resonance of the pulses used in the transition. The duration of each pulse is listed below the diagram. Each such sequence takes 600 ms.

a sinusoid processed to extract the resonance frequency $f_0(b\bar{b})$ [26]. The values of $f_0(b\bar{b})$ are separately recorded for the $\mathcal{D} = \pm 1$ ensembles and denoted as $f_0(b\bar{b}, \mathcal{D} = \pm 1)$.

The $b \leftrightarrow \bar{b}$ resonance frequency can be expressed as

$$f_0(b\bar{b}, \mathcal{D} = \pm 1) = 2Z_b \pm 2W_T \langle \vec{I} \cdot \hat{x} \rangle, \quad (4)$$

where Z_b is the Zeeman shift of the b state due to the applied magnetic field, and the P-odd T-odd quantity $\langle \vec{I} \cdot \hat{x} \rangle$ is the expectation value of the nuclear spin projection onto the direction of $\vec{\mathcal{E}}_{\text{eq}}$. Based on the Zeeman and hyperfine structure constants measured in Refs. [8, 9], we evaluate $|\langle \vec{I} \cdot \hat{x} \rangle| = 0.75$, see Supplemental Material Section II. The time-varying T-violating shift, $\delta W_T \equiv W_T - \text{avg}(W_T)$, and Zeeman shift, Z_b , determined from $f_0(b\bar{b}, \mathcal{D} = \pm 1)$, are shown as a function of measurement time in Fig. 4. As the interval between samples of δW_T is non-uniform (due to occasional laser frequency jumps and experiment pauses), we use the Lomb-Scargle periodogram [30] to determine its power spectral density.

The periodogram frequencies are sampled uniformly from 313 nHz (half the inverse of the experiment duration, $T_{\text{int}} = 1.59 \times 10^6$ s) to 74 mHz (half the inverse of the

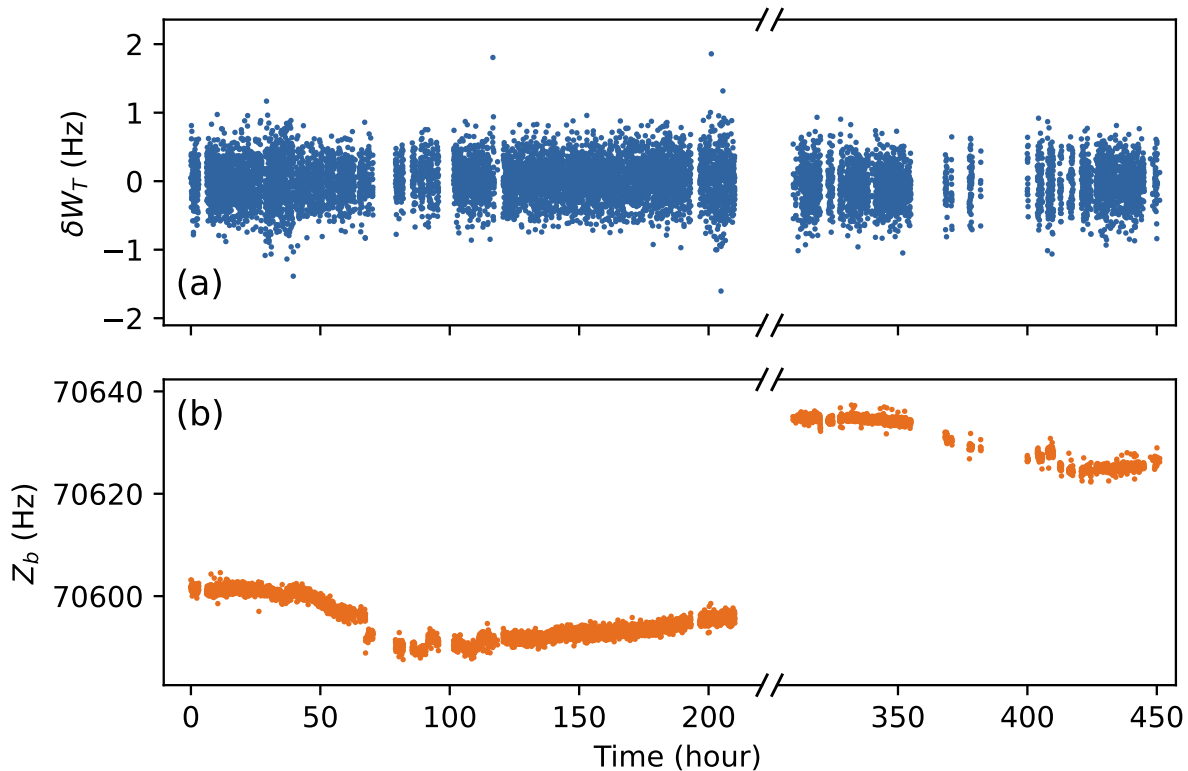


FIG. 4. (a) The time-varying T-violating frequency shift δW_T . (b) The Zeeman shift of the b state. Each point in the figure is data from one full experiment cycle. Fluctuations in the Zeeman shift are due to background magnetic field drifts. The Zeeman shift was separated from the ALP signal using the oppositely-polarized ion ensembles as comagnetometers [20]. The break inserted before the 300 hour mark was used to make a large deliberate change in the magnetic field, in order to test the ability of the comagnetometer comparison to reject magnetic field fluctuations.

experiment cycle time, $T_{\text{cycle}} = 6.7$ s) in 603316 steps. The power spectral density of δW_T is shown in Fig. 5. To determine the non-ALP background in the δW_T power spectrum, we split the spectrum into 10 log-spaced bins such that the noise power in each bin is approximately frequency-independent. As the ALP field is expected to be coherent with a quality factor of $\sim 10^6$ [31], the bandwidth of a possible ALP signal is much smaller than the bin bandwidth for each of the bins. Therefore, we use the average power in each frequency bin to build an exponential distribution to search for significant excess power due to ALP-induced oscillations. A 95% confidence level limit derived from the exponential distribution is shown in Fig. 5.

The 95% confidence limits on δW_T oscillations can be used to place a bound on

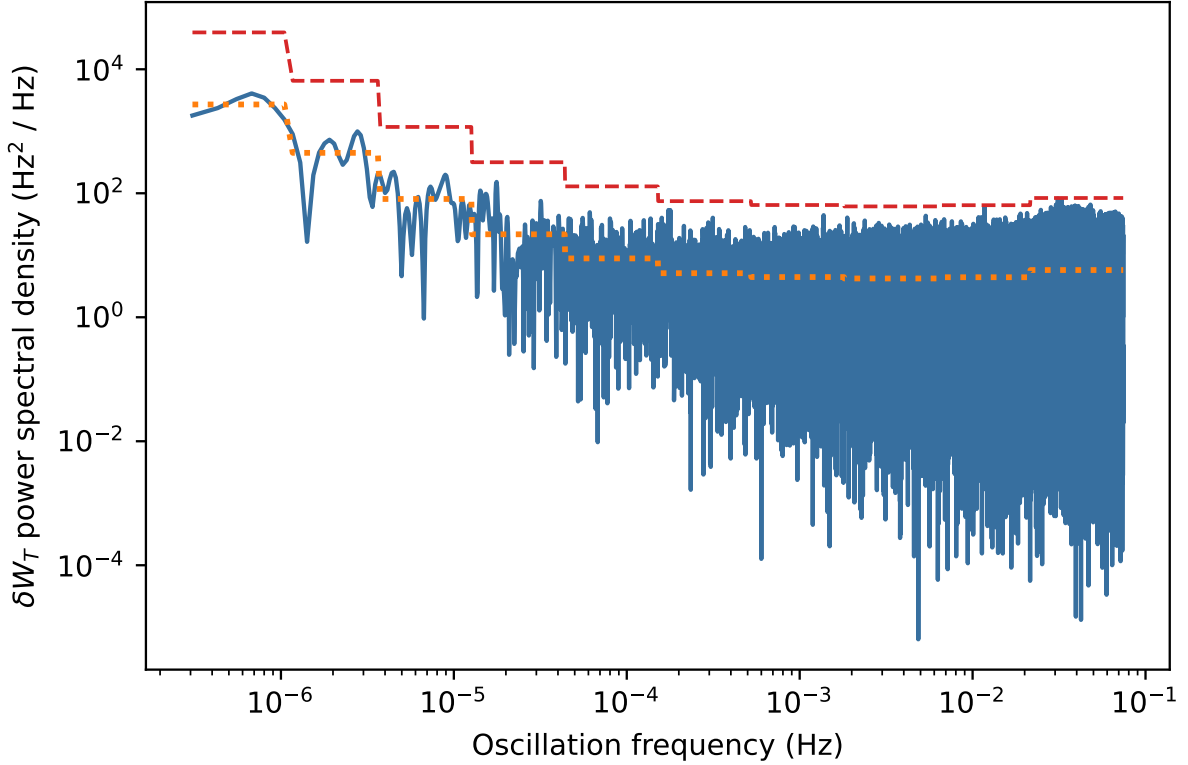


FIG. 5. Power spectral density of the T-violation frequency shift δW_T . The average of the binned power spectral density (orange, dotted line) and the 95% global confidence level constraint on δW_T oscillation (red, dashed line) are shown.

ALP-gluon coupling using Eq. 3. However, we have to consider corrections due to the experiment cycle time and the stochastic nature of the ALP field amplitudes [9, 32]. First, for oscillation frequencies comparable to or greater than $1/T_{\text{cycle}}$, the δW_T oscillation amplitudes would be underestimated due to downsampling in each experiment cycle. We generated sinusoidal data at different frequencies based on the experiment timestamps, accounting for the experiment cycle time, and computed the power spectrum at the measured frequencies. This yields a calibration curve for the experimental sensitivity as a function of oscillation frequency which is used to scale the δW_T exclusion range, similar to the method used in Ref. [9]. Second, the ALP coherence time is approximately 10^6 times the oscillation period, which is comparable to or greater than the measurement time used in this work for frequencies between $1/T_{\text{int}}$ and $1/T_{\text{cycle}}$. Therefore the ALP oscillations must be corrected for a stochastic bias. The ALP field amplitude, a_0 , follows a Rayleigh distribution whose root-mean-square

value is $a_{\text{DM}} = \sqrt{2\rho_{\text{DM}}(\hbar c)^3}/(m_a c^2)$, assuming the ALP is the dominant source contributing to local dark matter with density $\rho_{\text{DM}} = 0.4 \text{ GeV/cm}^3$ [8, 33]. We increase the deterministic model ALP-gluon coupling bound by a factor of 3 to account for stochasticity following Ref. [32]. The resulting bound, smoothed with a Savitzky-Golay filter for ease of visualization [34], is shown in Fig. 6. The value of $\mathcal{S}_{\bar{\theta}}$ that enters Eq. 3 was calculated to be 3.7 e fm^3 in Ref. [18] and 0.15 e fm^3 in Ref. [19]. We use the geometric mean of these two values, 0.74 e fm^3 , to construct the solid line for the exclusion plot shown in Fig. 6, and the difference between these values as the uncertainty band. This bound improves the constraints placed by previous atomic [10–16] and molecular [9] experiments.

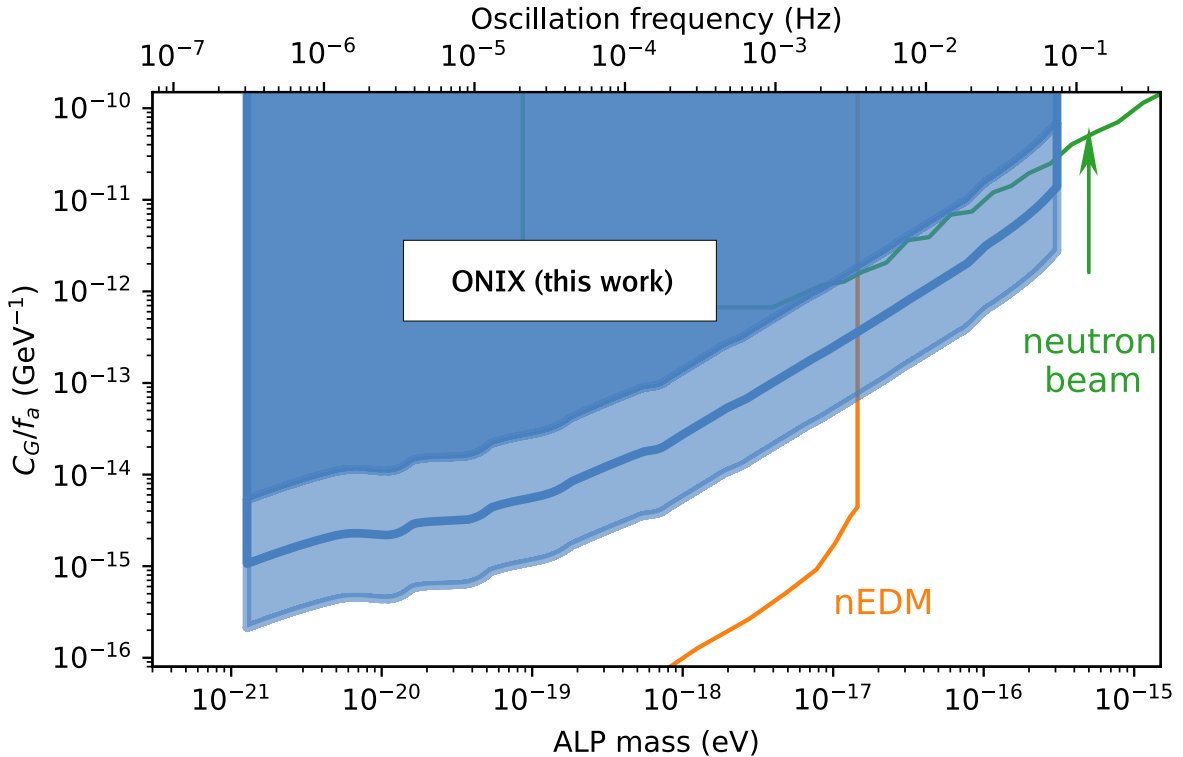


FIG. 6. 95% confidence exclusion range on the ALP-gluon coupling from this work. The uncertainty band around the exclusion limit is due to differing theoretical estimates of the nuclear Schiff moment of ^{153}Eu [18, 19]. Other laboratory constraints in this range of ALP masses use data from [35]: nEDM (orange, no stochastic correction applied) [7], neutron beam EDM (green, stochasticity corrected) [8].

In summary, we have performed precision measurements that constrain oscillatory

symmetry-violation in octupole-deformed nuclei in a crystal, leading to a broadband bound on the parameter space of axionlike dark matter. Higher experimental precision is anticipated in the future, from apparatus upgrades to increase the nuclear spin coherence time and reduce noise in the optical detectors. Our measurements also motivate nuclear structure experiments and calculations to resolve the theoretical uncertainty in $\mathcal{S}_{\bar{\theta}}$ for ^{153}Eu .

Acknowledgments. We thank Yoshiro Takahashi, Jonathan Weinstein, Eric Hessels and Andrew Jayich for helpful discussions. Julia Ford and Daniel Stedman contributed to the construction of the initial apparatus, and Harish Ramachandran made significant contributions to developing the T-violation search concept. Bob Amos and Paul Woitalla provided vital technical support. M.F. acknowledges funding from a CQIQC Postdoctoral Fellowship, and A.R. acknowledges funding from a CQIQC Undergraduate Summer Research Award. This project was enabled by support from the John Templeton Foundation (Grant No. 63119), the Alfred P. Sloan Foundation (Grant No. G-2023-21045), and NSERC (SAPIN-2021-00025).

-
- [1] Planck Collaboration: N. Aghanim et al. Planck 2018 results. *Astronomy & Astrophysics*, 641, 2020.
 - [2] Gianfranco Bertone and Tim MP Tait. A new era in the search for dark matter. *Nature*, 562(7725):51–56, 2018.
 - [3] Lam Hui. Wave dark matter. *Annu. Rev. Astron. and Astrophys.*, 59:247–289, 2021.
 - [4] Elisa G. M. Ferreira. Ultra-light dark matter. *The Astronomy and Astrophysics Review*, 29(1):7, December 2021.
 - [5] Francesca Chadha-Day, John Ellis, and David J. E. Marsh. Axion dark matter: What is it and why now? *Science Advances*, 8(8):eabj3618, February 2022.
 - [6] Y.V. Stadnik and V.V Flambaum. Axion-induced effects in atoms, molecules, and nuclei. *Phys. Rev. D*, 89(4):043522, 2014.
 - [7] C. Abel et al. Search for Axionlike Dark Matter through Nuclear Spin Precession in Electric and Magnetic Fields. *Physical Review X*, 7(4):041034, 2017.

- [8] Ivo Schulthess, Estelle Chanel, Anastasio Fratangelo, Alexander Gottstein, Andreas Gsponer, Zachary Hodge, Ciro Pistillo, Dieter Ries, Torsten Soldner, Jacob Thorne, and Florian M. Piegsa. New Limit on Axionlike Dark Matter Using Cold Neutrons. *Physical Review Letters*, 129(19):191801, November 2022.
- [9] Tanya S. Roussy, Daniel A. Palken, William B. Cairncross, Benjamin M. Brubaker, Daniel N. Gresh, Matt Grau, Kevin C. Cossel, Kia Boon Ng, Yuval Shagam, Yan Zhou, Victor V. Flambaum, Konrad W. Lehnert, Jun Ye, and Eric A. Cornell. Experimental Constraint on Axionlike Particles over Seven Orders of Magnitude in Mass. *Physical Review Letters*, 126(17):171301, April 2021.
- [10] A. Hees, J. Guéna, M. Abgrall, S. Bize, and P. Wolf. Searching for an Oscillating Massive Scalar Field as a Dark Matter Candidate Using Atomic Hyperfine Frequency Comparisons. *Physical Review Letters*, 117(6):061301, August 2016.
- [11] Colin J. Kennedy, Eric Oelker, John M. Robinson, Tobias Bothwell, Dhruv Kedar, William R. Milner, G. Edward Marti, Andrei Derevianko, and Jun Ye. Precision Metrology Meets Cosmology: Improved Constraints on Ultralight Dark Matter from Atom-Cavity Frequency Comparisons. *Physical Review Letters*, 125(20):201302, November 2020.
- [12] Takumi Kobayashi, Akifumi Takamizawa, Daisuke Akamatsu, Akio Kawasaki, Akiko Nishiyama, Kazumoto Hosaka, Yusuke Hisai, Masato Wada, Hajime Inaba, Takehiko Tanabe, and Masami Yasuda. Search for Ultralight Dark Matter from Long-Term Frequency Comparisons of Optical and Microwave Atomic Clocks. *Physical Review Letters*, 129(24):241301, December 2022.
- [13] Nathaniel Sherrill, Adam O Parsons, Charles F A Baynham, William Bowden, E Anne Curtis, Richard Hendricks, Ian R Hill, Richard Hobson, Helen S Margolis, Billy I Robertson, Marco Schioppo, Krzysztof Szymaniec, Alexandra Tofful, Jacob Tunesi, Rachel M Godun, and Xavier Calmet. Analysis of atomic-clock data to constrain variations of fundamental constants. *New Journal of Physics*, 25(9):093012, September 2023.
- [14] Xue Zhang, Abhishek Banerjee, Mahapan Leyser, Gilad Perez, Stephan Schiller, Dmitry Budker, and Dionysios Antypas. Search for Ultralight Dark Matter with Spectroscopy of Radio-Frequency Atomic Transitions. *Physical Review Letters*, 130(25):251002, June 2023.

- [15] Abhishek Banerjee, Dmitry Budker, Melina Filzinger, Nils Huntemann, Gil Paz, Gilad Perez, Sergey Porsev, and Marianna Safronova. Oscillating nuclear charge radii as sensors for ultralight dark matter, 2023.
- [16] Hyungjin Kim, Alessandro Lenoci, Gilad Perez, and Wolfram Ratzinger. Probing an ultralight QCD axion with electromagnetic quadratic interaction. *Physical Review D*, 109(1):015030, January 2024.
- [17] H. D. Ramachandran and A. C. Vutha. Nuclear T-violation search using octopole-deformed nuclei in a crystal. *Phys. Rev. A*, 108:012819, 2023.
- [18] V. V. Flambaum and H. Feldmeier. Enhanced nuclear Schiff moment in stable and metastable nuclei. *Phys. Rev. C*, 101(1):015502, January 2020.
- [19] O. P. Sushkov. Schiff moments of deformed nuclei. *Physical Review C*, 110(1):015501, 2024.
- [20] Bassam Nima, Mingyu Fan, Aleksandar Radak, and Amar Vutha. Comagnetometry using oppositely-polarized Eu^{3+} ions in a crystal. in preparation.
- [21] V. V. Flambaum and V. A. Dzuba. Electric dipole moments of atoms and molecules produced by enhanced nuclear Schiff moments. *Phys. Rev. A*, 101(4):042504, April 2020.
- [22] Flurin Könz, Y. Sun, C. W. Thiel, R. L. Cone, R. W. Equall, R. L. Hutcheson, and R. M. Macfarlane. Temperature and concentration dependence of optical dephasing, spectral-hole lifetime, and anisotropic absorption in $\text{Eu}^{3+}:\text{Y}_2\text{SiO}_5$. *Phys. Rev. B*, 68:085109, Aug 2003.
- [23] S. Zhang, N. Lučić, N. Galland, R. Le Targat, P. Goldner, B. Fang, S. Seidelin, and Y. Le Coq. Precision measurements of electric-field-induced frequency displacements of an ultranarrow optical transition in ions in a solid. *Appl. Phys. Lett.*, 117(22):221102, 2020.
- [24] Emmanuel Zambrini Cruzeiro, Jean Etesse, Alexey Tiranov, Pierre-Antoine Bourdel, Florian Fröwis, Philippe Goldner, Nicolas Gisin, and Mikael Afzelius. Characterization of the hyperfine interaction of the excited $^5\text{D}_0$ state of $\text{Eu}^{3+} : \text{Y}_2\text{SiO}_5$. *Phys. Rev. B*, 97:094416, Mar 2018.
- [25] R. M. Macfarlane and R. M. Shelby. Coherent transient and holeburning spectroscopy of rare earth ions in solids. In A. A. Kaplyanskii and R. M. Macfarlane, editors, *Spectroscopy of Solids Containing Rare Earth Ions*, volume 21, pages 51–184. 1987.

- [26] A. C. Vutha and E. A. Hessels. Frequency-offset separated oscillatory fields. *Physical Review A*, 92(5):052504, November 2015.
- [27] K. Kato, T. D. G. Skinner, and E. A. Hessels. Ultrahigh-precision measurement of the $n = 2$ triplet p fine structure of atomic helium using frequency-offset separated oscillatory fields. *Phys. Rev. Lett.*, 121:143002, 2018.
- [28] N Bezginov, T Valdez, M Horbatsch, A Marsman, AC Vutha, and EA Hessels. A measurement of the atomic hydrogen lamb shift and the proton charge radius. *Science*, 365(6457):1007–1012, 2019.
- [29] Ryuzi Yano, Masaharu Mitsunaga, and Naoshi Uesugi. Nonlinear laser spectroscopy of $\text{Eu}^{3+}:\text{Y}_2\text{SiO}_5$ and its application to time-domain optical memory. *Journal of the Optical Society of America B*, 9(6):992, June 1992.
- [30] Jacob T. VanderPlas. Understanding the Lomb–Scargle Periodogram. *The Astrophysical Journal Supplement Series*, 236(1):16, May 2018.
- [31] Joshua W. Foster, Nicholas L. Rodd, and Benjamin R. Safdi. Revealing the dark matter halo with axion direct detection. *Physical Review D*, 97(12):123006, June 2018.
- [32] Gary P. Centers, John W. Blanchard, Jan Conrad, Nataniel L. Figueroa, Antoine Garçon, Alexander V. Gramolin, Derek F. Jackson Kimball, Matthew Lawson, Bart Pelssers, Joseph A. Smiga, Alexander O. Sushkov, Arne Wickenbrock, Dmitry Budker, and Andrei Derevianko. Stochastic fluctuations of bosonic dark matter. *Nature Communications*, 12(1):7321, December 2021.
- [33] Riccardo Catena and Piero Ullio. A novel determination of the local dark matter density. *Journal of Cosmology and Astroparticle Physics*, 2010(08):004–004, August 2010.
- [34] Abraham Savitzky and M. J. E. Golay. Smoothing and Differentiation of Data by Simplified Least Squares Procedures. *Analytical Chemistry*, 36(8):1627–1639, July 1964.
- [35] Ciaran O’Hare. cajohare/AxionLimits: AxionLimits, July 2020.

I. EQUIVALENT ELECTRIC FIELD

Eu^{3+} ions are electrically polarized by their neighboring ions in the YSO crystal. The equivalent electric field, \mathcal{E}_{eq} , interacts with the permanent EDM of Eu^{3+} ions induced by the nuclear Schiff moment to produce the measured T-violating frequency shift W_T , as described in Eq. 3 in the main text.

To date, there have not been any calculations of \mathcal{E}_{eq} in Eu:YSO. The nuclear Schiff-moment-induced energy shift in $\text{EuCl}_3:6\text{H}_2\text{O}$ was calculated in Ref. [1], from which we can estimate \mathcal{E}_{eq} in $\text{EuCl}_3:6\text{H}_2\text{O}$. The value of \mathcal{E}_{eq} in Eu:YSO is then obtained by scaling the $\text{EuCl}_3:6\text{H}_2\text{O}$ equivalent electric field using the ratio of the experimentally-measured Stark shift coefficients of these two systems [2, 3].

In $\text{EuCl}_3:6\text{H}_2\text{O}$, the nuclear Schiff moment of ^{153}Eu shifts the ion energy levels by

$$\delta E_T = 3 \times 10^{-9} \theta \text{ eV}, \quad (\text{S1})$$

according to Ref. [1]. This energy shift is based on an estimated nuclear Schiff moment of $S = 5\theta \text{ e} \cdot \text{fm}^3$. The permanent electric dipole moment of the $^{153}\text{Eu}^{3+}$ ion induced by the nuclear Schiff moment is [4]

$$d_{\text{Eu}} = 0.33 \times 10^{-17} \text{ e} \cdot \text{cm} \frac{S}{\text{e} \cdot \text{fm}^3} = 1.7 \times 10^{-17} \theta \text{ e} \cdot \text{cm}. \quad (\text{S2})$$

From Eqs. S1 and S2, the equivalent electric field on the $^{153}\text{Eu}^{3+}$ ion in $\text{EuCl}_3:6\text{H}_2\text{O}$ is

$$|\mathcal{E}_{\text{eq}}(\text{EuCl}_3 : 6\text{H}_2\text{O})| = \left| -\frac{\delta E_T}{d_{\text{Eu}}} \right| = 0.18 \text{ GV cm}^{-1}. \quad (\text{S3})$$

The differential Stark shift coefficient for the ${}^7F_0 \rightarrow {}^5D_0$ optical transition is

$$\Delta\zeta \equiv -\frac{\delta(E({}^5D_0) - (E({}^7F_0)))}{\delta\mathcal{E}} = \Delta\alpha L \mathcal{E}_{\text{eq}}. \quad (\text{S4})$$

where $\Delta\alpha \equiv \alpha({}^5D_0) - \alpha({}^7F_0)$ is the differential dipole scalar polarizability of the ${}^7F_0 \rightarrow {}^5D_0$ transition, and $L = (\epsilon_r + 2)/3$ is a local field correction factor with ϵ_r being the relative permittivity of the crystal [5].

The relative permittivity is $\epsilon_r \approx 3.6$ in $\text{EuCl}_3 : 6\text{H}_2\text{O}$ [5] compared to $\epsilon_r = 9.36$ along

TABLE S1. Projections of the nuclear spin along the crystal D1 (\hat{x}), D2 (\hat{y}), and b (\hat{z}) axes.

	$\langle \vec{I} \cdot \hat{x} \rangle$	$\langle \vec{I} \cdot \hat{y} \rangle$	$\langle \vec{I} \cdot \hat{z} \rangle$
$ \bar{a}\rangle$	-1.48	-0.96	1.72
$ a\rangle$	1.48	0.96	-1.72
$ \bar{b}\rangle$	-0.75	-0.03	0.91
$ b\rangle$	0.75	0.03	-0.91
$ \bar{c}\rangle$	-0.05	0.20	0.33
$ c\rangle$	0.05	-0.20	-0.33

the crystal D1 axis in Eu:YSO [6]. The measured Stark shift coefficients are $\Delta\zeta = 1.57(2)$ kHz/(V/cm) in $\text{EuCl}_3:6\text{H}_2\text{O}$ [2], and $\Delta\zeta = 27.2(2)$ kHz/(V/cm) along the D1 axis in Eu:YSO. Therefore we estimate the component of $\vec{\mathcal{E}}_{\text{eq}}$ along the D1 axis in Eu:YSO to be

$$|\vec{\mathcal{E}}_{\text{eq}}(\text{Eu} : \text{YSO}) \cdot \hat{x}| = |\mathcal{E}_{\text{eq}}(\text{EuCl}_3 : 6\text{H}_2\text{O})| \left| \frac{\Delta\zeta(\text{Eu} : \text{YSO})}{\Delta\zeta(\text{EuCl}_3 : 6\text{H}_2\text{O})} \right| \frac{L(\text{EuCl}_3 : 6\text{H}_2\text{O})}{L(\text{Eu} : \text{YSO})} = 1.5 \text{ GV cm}^{-1}. \quad (\text{S5})$$

II. NUCLEAR SPIN PROJECTIONS

In this section we evaluate the Eu^{3+} nuclear spin projection along the crystal D1 axis, $\langle \vec{I} \cdot \hat{x} \rangle$, which is used in Eq. 4 of the main text. The hyperfine and Zeeman Hamiltonian for the nuclear spin degree of freedom in the ground 7F_0 electronic state in Eu:YSO is

$$\mathcal{H} = \vec{I} \cdot \mathbf{Q} \cdot \vec{I} + \vec{B} \cdot \mathbf{M} \cdot \vec{I}, \quad (\text{S6})$$

where $\vec{B} \approx 225 \text{ G} \cdot \hat{x}$ is the magnetic field, \mathbf{Q} is the quadrupole tensor, and \mathbf{M} is the gyromagnetic tensor [7]. The quadrupole tensor \mathbf{Q} for the ground 7F_0 electronic state of ${}^{153}\text{Eu}$:YSO is reported in Ref. [8]. The gyromagnetic tensor \mathbf{M} has only been measured for the 7F_0 state of ${}^{151}\text{Eu}$ ($I = 5/2$) in YSO [9]. We scale the ${}^{151}\text{Eu}$:YSO \mathbf{M} tensor by the ratio of the nuclear magnetic dipole moments of ${}^{153}\text{Eu}$ and ${}^{151}\text{Eu}$ [10], to estimate the \mathbf{M} tensor for ${}^{153}\text{Eu}$:YSO. The nuclear spin eigenstates are obtained from diagonalization of the above Hamiltonian. The projections of the nuclear spins along the $D1$, $D2$, and b dielectric axes of the crystal are shown in Table S1.

-
- [1] A. O. Sushkov, O. P. Sushkov, and A. Yaresko. Effective electric field: Quantifying the sensitivity of searches for new P,T-odd physics with $\text{EuCl}_3:6\text{H}_2\text{O}$. *Phys. Rev. A*, 107(6):062823, June 2023.
- [2] R. L. Ahlefeldt, D. L. McAuslan, J. J. Longdell, N. B. Manson, and M. J. Sellars. Precision Measurement of Electronic Ion-Ion Interactions between Neighboring Eu^{3+} Optical Centers. *Physical Review Letters*, 111(24):240501, December 2013.
- [3] S. Zhang, N. Lučić, N. Galland, R. Le Targat, P. Goldner, B. Fang, S. Seidelin, and Y. Le Coq. Precision measurements of electric-field-induced frequency displacements of an ultranarrow optical transition in ions in a solid. *Appl. Phys. Lett.*, 117(22):221102, 2020.
- [4] V. V. Flambaum and V. A. Dzuba. Electric dipole moments of atoms and molecules produced by enhanced nuclear Schiff moments. *Phys. Rev. A*, 101(4):042504, April 2020.
- [5] Rose Ahlefeldt. *Evaluation of a stoichiometric rare earth crystal for quantum computing*. PhD thesis, The Australian National University, 2013.
- [6] N. C. Carvalho, J-M. Le Floch, J. Krupka, and M. E. Tobar. Multi-mode technique for the determination of the biaxial Y_2SiO_5 permittivity tensor from 300 to 6 K. *Applied Physics Letters*, 106(19):192904, May 2015.
- [7] J. J. Longdell, M. J. Sellars, and N. B. Manson. Hyperfine interaction in ground and excited states of praseodymium-doped yttrium orthosilicate. *Physical Review B*, 66(3):035101, June 2002.
- [8] Ryuzi Yano, Masaharu Mitsunaga, and Naoshi Uesugi. Nonlinear laser spectroscopy of $\text{Eu}^{3+}:\text{Y}_2\text{SiO}_5$ and its application to time-domain optical memory. *Journal of the Optical Society of America B*, 9(6):992, June 1992.
- [9] Emmanuel Zambrini Cruzeiro, Jean Etesse, Alexey Tiranov, Pierre-Antoine Bourdel, Florian Fröwis, Philippe Goldner, Nicolas Gisin, and Mikael Afzelius. Characterization of the hyperfine interaction of the excited $^5\text{D}_0$ state of $\text{Eu}^{3+}:\text{Y}_2\text{SiO}_5$. *Phys. Rev. B*, 97:094416, Mar 2018.
- [10] N.J. Stone. Table of Nuclear Magnetic Dipole and Electric Quadrupole Moments. Technical Report INDC(NDS)–0658, International Atomic Energy Agency (IAEA), Vienna,

February 2014.